Journal of Materials Chemistry A

ROYAL SOCIETY OF CHEMISTRY

PAPER

View Article Online
View Journal

Cite this: DOI: 10.1039/d6ta00748a

Insights into the selective hydrogenation of cinnamaldehyde on low-loading Pd based catalysts

Anca G. Mirea,[a] Iuliana M. Chirică,[ab] Iulia C. Ciobotaru,[a] Cristian Radu,[a] Ştefan Neaţu,[a] Florentina Neaţu,[a] Mihaela Florea *[a] and Mihaela M. Trandafir*[a]

This study explores how catalysts containing a low palladium loading (0.5 wt%) contribute to the selective hydrogenation of cinnamaldehyde. High specific surface area (SSA) mesoporous (2 wt%) TiO_2 – SiO_2 (UVM-7) materials were prepared by two different approaches: a *one-step procedure*, in which titania and silica precursors were added from the beginning to generate Ti_2@UVM-7 support, and a *two-step procedure*, where TiO_2 was deposited onto the UVM-7 silica surface *via* wet impregnation technique (Ti_2/UVM-7). Both types of supports were decorated with Pd nanoparticles (NPs) through the deposition–precipitation technique. The obtained catalysts were thoroughly characterized by using different techniques, including XRD, N_2 adsorption–desorption isotherms at liquid N_2 temperature, ATR-FTIR, TEM-EDX, SEM-EDX, and XPS. Characterization data revealed that *one-step procedure* largely preserves the textural and structural properties of the support following the deposition–precipitation of the noble metal, whereas the *two-step procedure* slightly alters the UVM-7 morphology. Moreover, the preparation method of the supports impacts the Pd particle sizes and the metal-support interaction (MSI). The *one-step procedure* tends to promote the growth of larger Pd NPs, likely due to the TiO_2 species being well embedded within the SiO_2 matrix. In contrast, the *two-step procedure* yields well-dispersed Pd NPs smaller than 2 nm, due to the confinement of TiO_2 nanodomains within the UVM-7 cavities, which enhances the MSI. Consequently, enhanced catalytic performance and stability were achieved with 0.5Pd/Ti_2/UVM-7 (~99% hydrocinnamaldehyde yield, TOF 4.81 s^{-1}), due to the formation of very small Pd nanoparticles on the support that promote the MSI.

Received 26th January 2026
Accepted 13th April 2026

DOI: 10.1039/d6ta00748a

rsc.li/materials-a

1 Introduction

Chemoselective hydrogenation of α,β-unsaturated carbonyl compounds in heterogeneous catalytic systems remains challenging,[1] as conventional methods rely on hazardous stoichiometric reducing agents that generate waste.[2] Heterogeneous catalysts are preferred due to their recyclability and lower environmental impact, in line with green chemistry goals, especially since hydrogenation is widely used in pharmaceutical synthesis,[3] where more than 9% of the overall processes consist of hydrogenation/reduction reactions.[3]

Cinnamaldehyde (CAL) is a representative molecule within the class of α, β-unsaturated aldehydes and is primarily found in cinnamon bark, which makes up approximately 90% of the essential oil. The reduction of CAL yields three main reaction products: cinnamyl alcohol (COL), hydrocinnamaldehyde (HCAL) and hydrocinnamyl alcohol (HCOL) – see Scheme 1. All the main reaction products are widely used as flavouring agents, perfumes, fragrances or in the production of pharmaceutical intermediates and fine chemicals.[2,4–9] Among them, HCAL was found to be an essential intermediate in the preparation of hydrocinnamic acid, which is utilized in the synthesis of protease inhibitors used in the treatment of HIV.[6,10] Traditional HCAL synthesis routes are environmentally unfriendly,[2] increasing interest in catalytic alternatives. The reduction of the olefinic bond of CAL to produce HCAL is thermodynamically and kinetically favoured over the reduction of the carbonyl bond

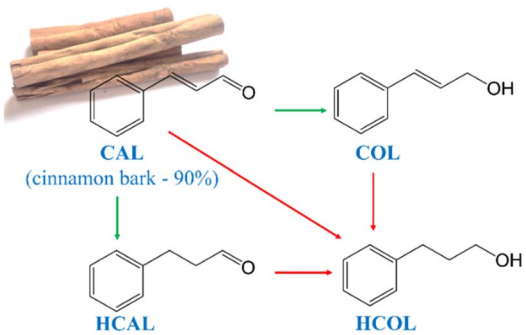

Scheme 1 Cinnamaldehyde hydrogenation – main reaction products.

[a]National Institute of Materials Physics, Atomistilor Street, 077125 Magurele, Ilfov, Romania. E-mail: mihaela.florea@infim.ro
[b]University of Bucharest, Faculty of Physics, 405 Atomistilor Street, 077125 Magurele, Romania

since it requires lower energy (about 35 kJ mol^{-1}) and is facilitated by the η^4 adsorption mode.[2,4,11–14] Even so, finding an active and selective catalyst is not an easy task since catalysts strongly depend on their design and structure, and are affected by electronic and geometric effects, as well as steric hindrance, among others.[2]

Non-noble metal-based catalysts (Ni, Cu, Co) are active in hydrogenation reaction of cinnamaldehyde,[2,15–17] but require harsh conditions (>150 °C, >30 atm H_2) and often show limited selectivity and stability.[18]

The reviews published in 2020 (ref. 2) or 2023 (ref. 19) present several noble and non-noble metals used as catalysts for the selective hydrogenation of CAL. Herein, noble metal-based catalysts containing Ir, Pt or Ru, which are metals with relatively large d-bandwidth, are recognized for their selectivity in COL production through the hydrogenation of CAL. The presence of larger radial expansion of the d orbitals increases the Pauli repulsion, thereby diminishing C=C adsorption, as C=C coordination is sensitive to this repulsion.[13] In opposition, Pd has more contracted d orbitals, facilitating the molecule access to the surface; thus, a η^4 adsorption mode is preferred, resulting in higher yield of HCAL.[13] Pd-based catalysts are often used as monometallic catalysts for the hydrogenation of CAL, due to their very good substrate conversion and selectivity towards HCAL; a 100% HCAL yield being reported by Chen *et al.*[20] However, a large amount of Pd is required (2 wt%). It is worth mentioning that ammonia borane (NH_3BH_3) was used as a reducing agent in the synthesis of the catalysts and the authors reported a gradual increase in the activity of their catalysts when the quantity of NH_3BH_3 was raised from 5 mg to 40 mg. A similar behaviour was evidenced in 2020 by Hu *et al.*[21] for Pd/$NiCo_2O_{4-x}$ catalysts (99.9% CAL conversion and HCAL selectivity, TOF 0.04 s^{-1}), where the HCAL selectivity was improved by increasing the $NaBH_4$: Pd molar ratio during the catalyst preparation step, ranging from 1 : 1 to 27 : 1, with the optimal result observed at a 27 : 1 molar ratio. These results indicate that not only the catalysts, but also the reducing agents might influence the catalytic performance, therefore the amount of reducing agent that reaches the catalytic process should be evaluated, since its recuperation involves additional purification steps.

As already mentioned, choosing the appropriate support is also crucial to designing active and selective catalysts, since the metal-support interaction (MSI) that stabilizes the metal NPs and prevent sintering or the electronic transfer from the support to the active metal plays an important role in the η^4 adsorption mode of the molecule on the catalyst surface.[12,22,23] Recently, Li *et al.*[24] reported that on the same catalyst (Pd_{SA+C} g^{-1}-C_3N_4), Pd single atoms cooperate with Pd clusters for selective hydrogenation of CAL to HCAL. Hydrogen preferentially adsorbs and dissociates on the Pd clusters and then overflow to further hydrogenate CAL, which preferentially adorbs on the Pd single atom catalyst. Their results indicate an impressive TOF of 9.19 s^{-1}; however, with a maximum HCAL selectivity of 97.3%.

For this study, mesoporous silica, UVM-7, after decoration with TiO_2 nanodomains was used as support for the preparation of 0.5 wt% Pd containing catalysts, which were further used for CAL chemoselective hydrogenation, employing ethanol as an environmentally friendly solvent. The use of UVM-7 as support for the synthesized catalysts was established based on its particular properties, such as high surface area, pore accessibility. UVM-7 can be regarded as a nanoscaled MCM-41-type material that, in addition to its intrinsic mesoporosity, exhibits a secondary network of larger textural pores formed through the aggregation of primary particles, resulting in a hierarchical pore architecture.[25] If the highly ordered and uniform pore system of MCM-41 can impose diffusion limitations, particularly for relatively bulky molecules,[26] the lower degree of structural ordering in UVM-7 is advantageous for catalytic applications, as it enhances mass transport, facilitate the diffusion of reactants through the pores and improve the dispersion of both titanium dioxide and noble metal on its surface. In this way, substrate still have access to the catalytically active centres during the reaction,[27] while TiO_2 was used to strengthen the MSI.

Two strategies were adopted for the decoration of the UVM-7 with TiO_2 nanodomains: (a) a *one-step procedure*, in which TiO_2 and UVM-7 were synthesized together, and (b) a *two-step procedure*, in which TiO_2 was deposited *via* impregnation following the preparation of UVM-7. The deposition–precipitation method was employed to achieve a low noble metal loading of 0.5 wt% Pd on the UVM-7-based support. This study examined the influence of several parameters, such as reaction time and preparation method of the support on activity, selectivity, and catalytic stability in the chemoselective CAL hydrogenation reaction.

2 Results and discussion

2.1 Catalyst characterization

2.1.1 XRD results. XRD patterns of the synthesized materials are presented in Fig. 1. UVM-7 mesostructured silica is an amorphous material characterized by an intense diffraction line and a shoulder at low 2θ values (2° and 3.8°, respectively), which correspond to the (100), (110) and (200) overlapped reflections of the hexagonal unit cell of the UVM-7 like materials, respectively (Fig. 1a and b).[28,29] The small angle XRD patterns of the Ti_2/UVM-7 and Ti_2@UVM-7 materials indicate that the specific structure of UVM-7 support was preserved in both preparation procedures (Fig. 1a and b). No additional lines corresponding to TiO_2 were identified. The intensity of the UVM-7 specific diffraction lines decreases after noble metal deposition on the support prepared by *one-step procedure* (Ti_2@UVM-7) as depicted in Fig. 1a and completely disappear for the *two-step procedure* (Ti_2/UVM-7) prepared materials (Fig. 1b), most probably due to the phase cancellation phenomenon induced by the noble metal NPs into the pore voids or a partial collapse of the structure, as previously reported by others.[23,30,31] The same phenomenon is observed when Pd is deposited directly onto UVM-7, the shoulder from 3.8° completely disappeared (red curve, Fig. 1b).

For all studied samples, the XRD diagrams were registered also in the high-angle range, and the results are presented in

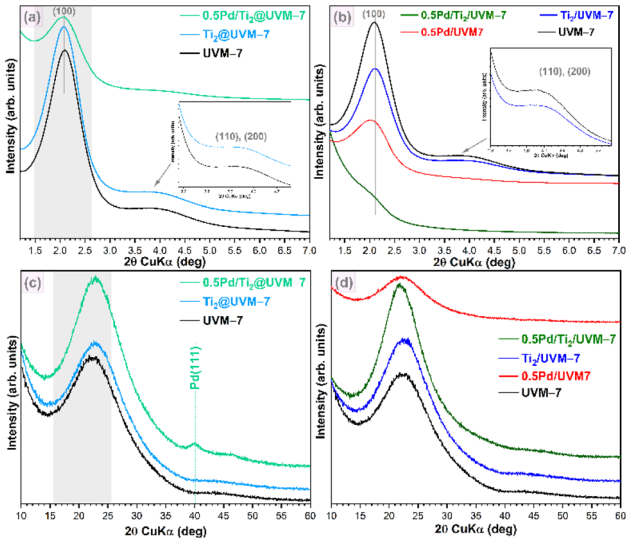

Fig. 1 X-ray diffraction patterns recorded at (a) small angle for Ti_2@UVM-7 based catalysts, (b) small angle for Ti_2/UVM-7 based catalysts, (c) high-range for Ti_2@UVM-7 based catalysts, and (d) high-range for Ti_2/UVM-7 based catalysts.

Fig. 1c and d. The catalyst containing Pd deposited by *one-step method* (0.5Pd/Ti_2@UVM-7) presents a peak at 40.16° corresponding to metallic palladium,[29] indicating the efficiency of the reduction step. The average size of the noble metal nanoparticles was calculated using the Scherrer method for the Pd (111) diffraction line and the value is presented in Table S1. It is important to note that for 0.5Pd/Ti_2/UVM-7 catalyst, there is no diffraction line corresponding to the noble metal or PdO, indicating that the possible presence of metal NPs is most likely below the XRD detection limits and/or very well dispersed. Also, no Pd or PdO specific lines were evidenced for 0.5Pd/UVM-7 catalyst (red curve in Fig. 1d) or 0.5Pd/TiO_2 catalyst (Fig. S1).

2.1.2 FTIR spectra. The FTIR spectra of the catalysts are gathered in Fig. S2 and confirm the silica structure. Since silica is the major component of the catalysts, the typical UVM-7 silica IR bands remain the most intense. The peaks observed at 1050–1075 cm^{-1} and 1230–1250 cm^{-1} are attributed to the two asymmetrical stretching (AS) vibrations of bridging oxygen: in-phase (AS_1, the adjacent oxygen atoms move in-phase with each other) and out-of-phase (AS_2, the adjacent oxygen atoms are out of phase), respectively. The peaks at 800–803 cm^{-1} and 978 cm^{-1} correspond to υS (Si–O–Si) and υS (Si–OH) vibrational modes, respectively.[28,32] The Pd–Ti– and Ti–containing UVM-7-based materials exhibit variations in Si–O–Si asymmetry stretching, with peaks appearing at 945–975 cm^{-1} which are associated with the stretching vibration of Ti–O–Si bond.[33] These changes are therefore likely to occur as a result of incorporation of TiO_2 or noble metal nanoparticles into the UVM-7 frameworks.

2.1.3 N_2 adsorption and desorption isotherms at −196 °C. The evolution of the mesostructure after different preparation steps is evidenced by the N_2 adsorption–desorption isotherms at −196 °C and are presented in Fig. S3. While ideal MCM-41 typically exhibits a type IV isotherm without a hysteresis loop due to its uniform cylindrical mesopores, the UVM-7 like materials present type IV isotherms with two adsorption steps, where the first adsorption step (P/P_0 < 0.5) is attributed to capillary condensation of N_2 inside the intraparticle mesopores, while the second one (P/P_0 > 0.8) is assigned to the texturally large interparticle voids[34] characteristic of hierarchical mesoporous structures.

According to the BET formalism, the UVM-7 support has a specific surface area (SSA) of 1076 $m^2\ g^{-1}$. The sample obtained by *one-step procedure* Ti_2@UVM-7 shows also type IV adsorption–desorption isotherms with two adsorption steps and a calculated SSA of 1091 $m^2\ g^{-1}$, which is comparable with as-prepared UVM-7 silica. These observations can infer that Ti species are well distributed into the silica walls for the *one-step procedure* and are in good agreement with FTIR spectra, where the formation of Ti–O–Si bonds was evidenced. The impregnation of the UVM-7 with TiO_2 led to a decrease of the SSA of the final material *i.e.*, Ti_2/UVM-7, by about 10% compared with as-prepared UVM-7 (see Table 1), probably due to the presence of the TiO_2 domains inside the mesopores. Herein, it can be attested the presence of a narrower H1 hysteresis loop compared with those measured for UVM-7 and Ti_2@UVM-7 supports, as a consequence of the pore necking effect of the TiO_2 species inside the mesopores, a fact observed also by others.[30] However, after the addition of TiO_2 (*one-step* or *two-step procedure*), the shape of the adsorption isotherms is comparable for both supports, confirming the preservation of bimodal porosity specific for UVM-7 like materials, which agrees also with the XRD results.

From the shape of the N_2 adsorption–desorption isotherms of the Pd containing catalyst prepared by the *one-step procedure*,

Table 1 BET surface area, pore size and volume of the UVM-7 based materials

Entry	Material	BET surface area ($m^2\ g^{-1}$)	BJH average pore size (nm)	BJH pore volume ($cm^3\ g^{-1}$)
1	Ti_2@UVM-7	1091	8.2	2.6
2	0.5Pd/Ti_2@UVM-7	1060	7.8	2.3
3	UVM-7	1077	6.5	2.1
4	Ti_2/UVM-7	970	8.4	2.4
5	0.5Pd/UVM-7	779	10.1	2.0
6	0.5Pd/Ti_2/UVM-7	363	22.4	1.7
7	TiO_2	47	76.5	0.8
8	0.5Pd/TiO_2	45	36.8	0.5

one can assume that the textural properties of the support are preserved, and therefore, the decrease of the SSA is only about 3% for 0.5Pd/Ti_2@UVM-7 compared to the support. All these observations are well correlated with the results obtained from the XRD investigations (Fig. S3) for structural data.

The noble metal deposition on the *two-step procedure* support leads to significant changes (Fig. S3). The first adsorption step completely disappears and only the sharp adsorption step at $P/P_0 > 0.8$ is preserved. This can be associated with partial support degradation but also with the intraparticle pore blockage, most probably due to the presence of Pd NPs at the entrance of the neck pores, because of the necking effect highlighted above. The SSA of the 0.5Pd/Ti_2/UVM-7 catalyst decreases up to 363 $m^2\ g^{-1}$ (see Table 1) meaning a decrease of about 63% compared with the Ti_2/UVM-7 support.

The average pore size calculated for the *two-step procedure* materials increases after the TiO_2 impregnation or/and Pd NPs deposition, from 6.5 nm (UVM-7) up to 22.4 nm for 0.5Pd/Ti_2/UVM-7 (see Table 1). Although noble metal deposition produces changes in the mesostructure and there is an abundance in larger intraparticle pores ($P/P_0 > 0.75$), the surface area is still high (363 $m^2\ g^{-1}$) and a significant proportion of small mesopores coexist ($P/P_0 < 0.5$), making the material suitable as catalyst.

The SSA of 0.5Pd/UVM-7 is 779 $m^2\ g^{-1}$, showing a 28% decrease in the SSA compared with the surface of the starting material UVM-7. The adsorption–desorption isotherm gathered in Fig. S3 is characteristic of mesoporous materials as UVM-7 with bimodal pore distribution, meaning that the features of UVM-7 like materials were preserved.

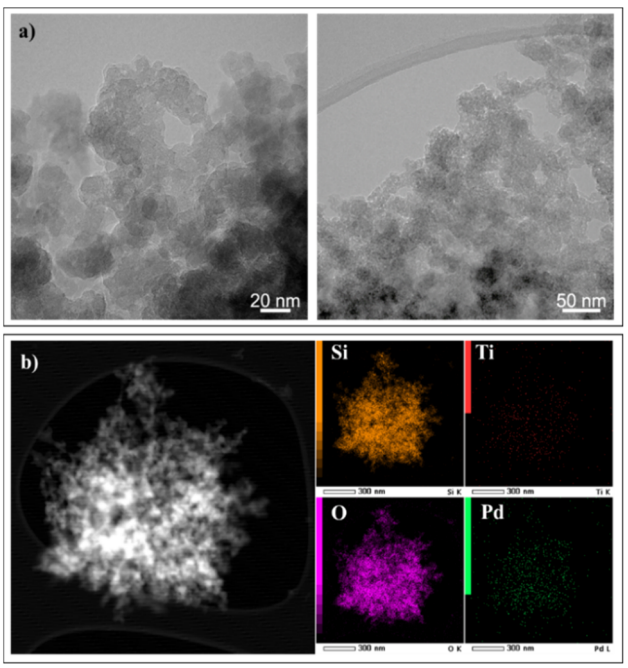

Fig. 2 (a) TEM images of the sample 0.5 Pd/Ti_2/UVM-7 and the histogram showing the size distribution of the Pd nanoparticles and (b) STEM dark field images and EDX mapping of the 0.5Pd/Ti_2/UVM-7 showing the elemental distribution of Si, O, Pd, Ti.

As expected, the TiO_2 P25 from Degussa displays a small SSA that is maintained after the Pd deposition (see entries 7 and 8 in Table 1).

2.1.4 TEM. TEM images of Pd based catalysts are shown in Fig. 2a, S4a, S5a and S5b and reveal that the typical architecture of the UVM-7 silica (the core of the composite) is generally preserved, attested by the presence of both structural mesopores and the existence of pores formed between nanoparticles.[28]

Pd NPs were clearly identified on the surface of the catalyst containing the *one-step preparation* support strategy, and their distribution is presented in Fig. S4a (inset). Herein, Pd NPs with a size ranging from 3–7 nm are the most abundant, although larger particles around 14 nm were also identified. These results are consistent with the XRD data, which indicates the presence of ~8 nm Pd NPs (see Table 1, entry 2).

When Pd is deposited on the *two-step preparation* support, the obtained nanoparticles are too small to be identified by TEM images (Fig. 2a). Nonetheless, they are clearly revealed by the dark field images and/or the corresponding EDX mapping (see Fig. 2b), showing excellent dispersion with particle sizes smaller than 2 nm. This supports the XRD results, where Pd NPs were not detected due to the detection limit (see Table 1, entry 6).

The deposition of Pd on as-prepared UVM-7 support generates larger Pd particles in the 0.5Pd/UVM-7 catalyst, with Pd particle sizes ranging from 1 to 33 nm (see Fig. S5), indicating that TiO_2 might be necessary to prevent Pd sintering on the surface of UVM-7 support.

The corresponding EDX maps (Fig. 2b, S4b, S5c and S5d) certify that Si, O and/or Ti are uniformly distributed through the material; herein, Pd NPs are also evidenced.

2.1.5 SEM-EDX. The chemical composition (atomic %) of the investigated catalysts was also determined by SEM-EDX and the data are gathered in Table S2. EDX was used to establish the amount of Ti incorporated into the framework by using the two preparation methods, together with the noble metal content and also to check the chemical homogeneity of the prepared solids. EDX data show that the prepared catalysts have a good chemical homogeneity (see Table S2). The measured Ti content is higher compared with the calculated one for the samples prepared by *one-step procedure* (see Si/Ti molar ratio in Table S2), as a consequence of the presence into the starting precursor solution of a certain portion of soluble Si-based oligomers which are removed during the preparation stage, leading to an indirect Ti species enrichment.[30] For the catalysts prepared by *two-step procedure*, the titanium content is lower, with values comparable with the nominal one (see Si/Ti molar ratio in Table S2); similar behaviour was reported by Moragues *et al.*[30]

2.1.6 XPS. XPS analyses of samples modified with Ti followed by Pd deposition are presented in Fig. 3, and the elemental composition of the surface is presented in Table S3.

The Ti 2p XPS spectra have been recorded for all prepared samples, and two components can be observed: one characteristic for Ti^{4+} (TiO_2) at 458.5 eV and a second one at higher energy (460.2 eV), which can be assigned to the TiO_2–SiO_2 interaction. Such behaviour was also been observed by Fernandez *et al.*[35] for TiO_2 clusters supported on a silica substrate

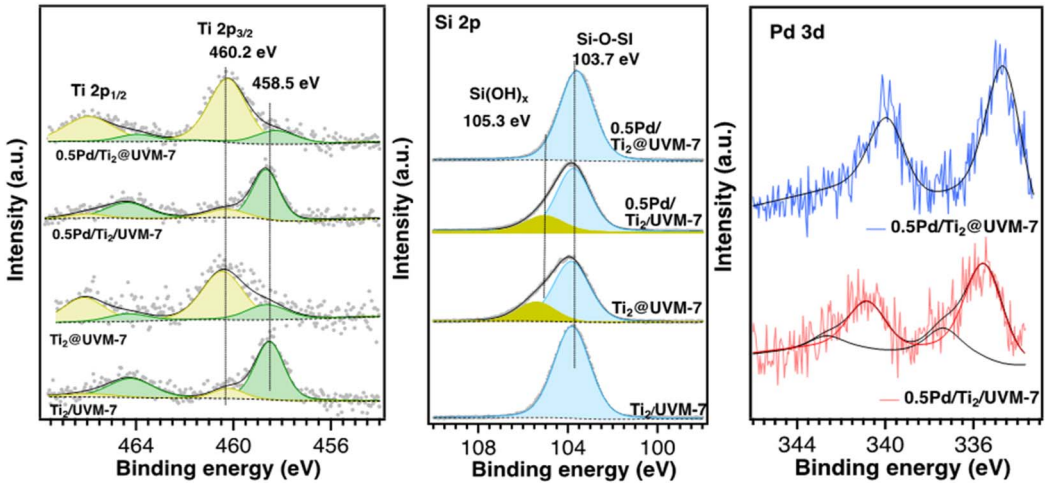

Fig. 3 Ti 2p, Si 2p and Pd 3d XPS high resolution spectra of Ti_2@UVM-7 and Ti_2/UVM-7 supports and after Pd deposition.

and which have observed badly ordered quasi-bidimensional arrangements of TiO_6 (octahedral) with some oxygen shared with SiO_2 support, that generated a less polarizable interface, inducing an increase in the effective positive charge of Ti and, therefore, a shift of the binding energy at higher energy. The preparation method is very important in generating different proportions between the two Ti components. The support prepared by *two-steps procedure* (Ti_2/UVM-7) has as main Ti component in TiO_2 form, and a small component of Ti–O–Si, while in the case of the *one-step preparation* method (Ti_2@UVM-7), Ti–O–Si is the predominant component. This suggests a clearer Ti–SiO_2 interaction in the *one-step procedure* method (Ti_2@UVM-7), where Ti is better integrated into the silica matrix, in contrast to the *two-step procedure* method (Ti_2/UVM-7), which mainly contains TiO_2 with limited Ti–O–Si bonding. The addition of Pd does not change the ratio between the Ti–O–Ti/Ti–O–Si components, independent of the adopted preparation procedure. It can be noted that the concentration of Si and Ti on the surface is significantly lower when the *one-step procedure* is employed (Table S3). Moreover, from Pd 3d core level depicted in Fig. 3, is observed that the method used to prepare the supports induces different oxidation states of Pd. Thus, using the *one-step procedure*, the catalyst maintains a lower oxidation state of Pd(0), in agreement with X-ray diffraction data, while the *two-step procedure* method favours the oxidation of Pd, where a second component with a higher binding energy (337.4 eV) is observed, which can be assigned to PdO.[36,37] However, for the *two-step procedure* catalyst, the peaks corresponding to Pd(0) are shifted to higher BE values, confirming a strong MSI[38] and are often associated with the presence of metal nanoparticles with very low particle sizes, as is the case of 0.5Pd/Ti_2/UVM-7 material.

In the case of Si 2p core level, two components were identified: a main component corresponding to Si–O–Si bonds and a second one at higher binding energies (105.3 eV), most likely associated with hydroxyl groups bonded to silicon.[39] No Si–O–Ti species at lower binding energies (~102 eV) were observed,[40] most probably due to the low ratio of Ti/Si at the surface (~0.01). Only the Ti_2@UVM-7 support, prepared by the *one-step procedure*, shows visible hydroxyl species on the surface, which disappear after Pd deposition, evidencing that these species were involved in binding Pd. In contrast, Pd deposition on the support prepared by the *two-step procedure* (Ti_2/UVM-7) leads to the formation of $Si(OH)_x$ species on the surface, possibly due to surface hydrolysis or rearrangement triggered by the deposition process on a differently structured surface. Overall, the *two-step procedure* method (Ti_2/UVM-7) results in a more oxidized and hydroxylated surface compared to the *one-step procedure*. This is evidenced by the formation of $Si(OH)_x$ species after Pd deposition and the presence of oxidized Pd species (PdO). These features suggest that the *two-step procedure* creates a surface environment more prone to hydrolysis and oxidation, likely due to a less integrated Ti in the SiO_2 matrix.

2.1.7 NH_3-TPD. The acidic properties of the considered supports were evaluated through NH_3-TPD and the desorbed NH_3 species evolution is shown in Fig. S6. All the investigated UVM-7 supports contain weak acid sites, as attested by NH_3 desorption around 180 °C. While UVM-7 support presents only weak acid sites, Ti_2/UVM-7 and Ti_2@UVM-7 have also acidic sites of medium strength, for which NH_3 desorption occurs at 300 °C and 395 °C, respectively. The increase in the strength of the acidity of Ti_2@UVM-7 likely arises from a more homogeneous incorporation of Ti species into the silica network during synthesis, leading to a higher proportion of dispersed TiO_6 units, as confirmed by XPS analysis. These species contribute to the formation of stronger and more numerous Lewis acid sites.[41] In comparison, commercial Degussa TiO_2 exhibits lower acidity than the UVM-7 silica-based supports (see Fig. S6).

2.1.8 Solid state NMR. The local silicon environment and the degree of framework condensation for the pure and Ti-modified UVM-7 materials were investigated using ^{29}Si MAS NMR spectroscopy. The resulting spectra and their corresponding deconvolution into Q^n species ($Q^n = Si(OSi)_n(OH)_{4-n}$) are shown in Fig. S7–S9. The ^{29}Si MAS NMR spectra of all samples display three distinct resonances characteristic of mesoporous silica frameworks, corresponding to Q^2 (geminal

silanols, $\delta \approx -91$ ppm), Q^3 (single surface silanols, $\delta \approx -101$ ppm), and Q^4 species (fully condensed tetrahedral siloxane units $\delta \approx -109$ to -112 ppm). Upon incorporation of titanium, a systematic downfield shift (deshielding) of the Q^4 resonance is observed, indicating modification of the silicon electronic environment due to the presence of Ti atoms. This effect is consistent with the formation of Si–O–Ti linkages, where substitution or coordination by less electronegative Ti perturbs the local electron density around silicon (Table S4).[42]

Comparative analysis of the spectra reveals that all materials retain the characteristic mesoporous silica structure; however, the mode of Ti incorporation significantly influences the local framework organization. The pure UVM-7 sample shows a highly condensed network, with a Q^4 resonance centered at $\delta \approx -112.18$ ppm and a noticeable Q^3 contribution associated with surface silanol groups. For the sample obtained by *two-step procedure* method, only a slight downfield shift of the Q^4 signal to $\delta \approx -111.47$ ppm is detected, suggesting that titanium species are predominantly anchored to surface silanol sites, with minimal impact on the bulk silica framework. In contrast, the material obtained by *one-step procedure* method exhibits a markedly different spectral profile. The Q^4 resonance shifts significantly to $\delta \approx -109.97$ ppm and displays pronounced line broadening, indicative of increased structural disorder. This substantial deshielding, together with the broadened signal, supports the isomorphic substitution of Si^{4+} by Ti^{4+} within the silica network and confirms the effective incorporation of titanium into the tetrahedral framework during synthesis. Consequently, a higher density of Si–O–Ti linkages is achieved compared to the post-synthetic impregnation approach.[42]

These results demonstrate that while both methods successfully introduce titanium into UVM-7 materials, *one-step procedure* enables a more homogeneous distribution of Ti within the framework walls, whereas impregnation primarily modifies the surface silanol environment without significantly altering the core silica structure.

2.2 Catalytic activity

2.2.1 General aspects. The reaction products obtained during CAL hydrogenation in the presence of the investigated catalysts using ethanol as solvent are depicted in Scheme 2, as follows: cinnamyl alcohol (COL), hydrocinnamaldehyde (HCAL), hydrocinnamyl alcohol (HCOL), cinnamaldehyde diethyl acetal (CDA) and hydrocinnamaldehyde diethyl acetal (HCDA). The catalytic performances of the proposed catalysts were analyzed considering (i) the influence of the reaction time and (ii) the contribution of the support.

Catalytic tests carried out in the absence of the catalyst (blank tests – 24 h) show that the substrate is transformed, in the reaction conditions, to CDA with a conversion of approximately 14% (see Table S5, Entry 1; reaction (**1**) from Scheme 2). Aldehyde diethyl acetals are formed due to the reaction between aldehydes and alcohols (acetalization reactions), such as cinnamaldehyde or hydrocinnamaldehyde and ethanol.[43] When mesoporous UVM-7 or TiO_2-modified supports were used as catalysts, a moderate increase of the conversion was observed,

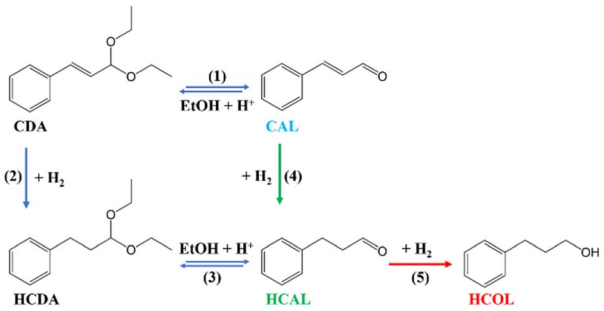

Scheme 2 Reaction pathways in the hydrogenation of cinnamaldehyde.

with UVM-7 yielding about 26% CAL conversion to CDA, while TiO_2-modified supports achieving slightly higher conversion of 28–31% to CDA (Table S5, Entries 2–4). These findings indicate that the acidic properties of the UVM-7 containing supports, as demonstrated by NH_3-TPD adsorption profiles, make them active for the acetalization of CAL. It is important to note that the support does not participate in the catalytic hydrogenation of CAL, as no such reaction products were identified.

Upon closer examination of Scheme 2, it can be summarized that the acetalization reaction of CAL leading to CDA or HCAL to HCDA is favored by: (i) the use of catalysts with acidic properties,[44] *i.e.*, the support used in the synthesis of the investigated catalysts (namely SiO_2) exhibits mildly acidic properties; (ii) the heterolytic dissociation of H_2 in the presence of metal oxide-containing catalysts (in this case TiO_2), generating active hydride species (H^-) and protons (H^+);[23] (iii) the presence of alcohol (*i.e.*, ethanol).

It is worth mentioning that the literature data[44–46] indicate that the acetalization reaction of the aldehydes (CAL and HCAL) is reversible in the presence of catalysts with acidic properties (see reaction (**1**) or reaction (**3**) from Scheme 2).

2.2.2 Influence of the reaction time on the catalytic performance. Fig. 4a, b and Table S6 present the conversion and product selectivity (including all identified compounds) for 0.5 wt% Pd deposited on both *one-step* and *two-step* prepared supports, highlighting both the catalytic performance and time-dependent evolution relevant to the HCAL reaction pathway.

The 0.5Pd/Ti_2@UVM-7 catalyst needs a longer induction period, as only 37% of CAL is transformed after 1 h, as depicted in Fig. 4a. At this stage, CDA is detected with 26% selectivity. After 2 h of reaction, the substrate is completely transformed, CDA vanishes, while HCDA selectivity increases and HCAL selectivity is maintained. These observations suggest a competition between two parallel reactions *i.e.*, hydrogenation and acetalization, that evolves as a new product formed in the reaction medium. In the first hour, there is competition between reaction (**4**), CAL to HCAL, and reaction (**1**), CAL to CDA. In the following hours, reaction (**2**), CDA to HCDA, competes with reaction (**3**), HCAL to HCDA.

Consequently, after 4 h reaction time, a quick increase in HCDA selectivity can be observed due to the subsequent hydrogenation of CDA to HCDA (reaction (**2**)) on one hand, and

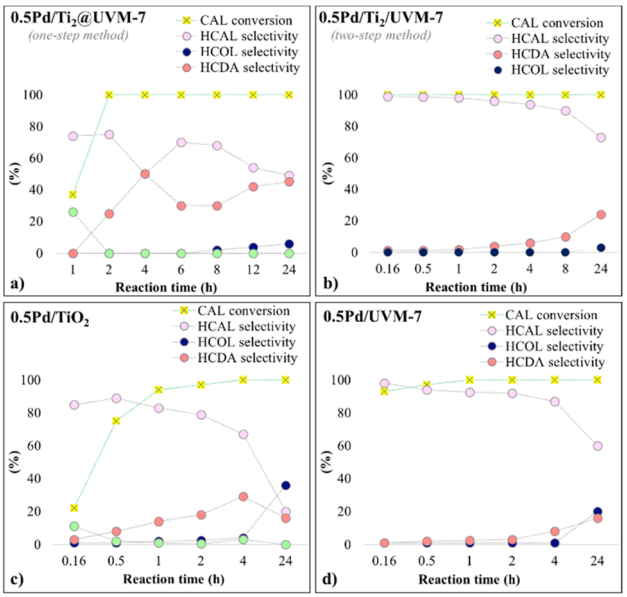

Fig. 4 Catalytic performance evolution with time (CAL conversion and products selectivity) for the investigated catalysts (a) 0.5Pd/Ti_2@UVM-7 prepared by *one-step procedure* support, (b) 0.5Pd/Ti_2/UVM-7 prepared by *two-step procedure* support, (c) 0.5Pd/TiO_2 and (d) 0.5Pd/UVM-7.

acetalization of HCAL (reaction (**3**)), on the other, for the 0.5Pd/Ti_2@UVM-7 catalyst (Fig. 4a). Between the 2nd and 6th hours of reaction, only the reversible reaction (**3**) between HCAL ↔ HCDA occurs. It can also be observed that the reaction tends towards equilibrium between the two species (HCAL and HCDA), reaching 50%–50% selectivity after 24 h in the presence of Pd/Ti_2@UVM-7 catalyst (Fig. 4a). After 8 h, as the reaction approaches equilibrium, HCOL starts to appear as the hydrogenation product of HCAL (reaction (**5**) in Scheme 2).

The 0.5Pd/Ti2/UVM7 catalyst is highly active (Fig. 4b), showing an outstanding selectivity towards hydrogenation reaction (∼99% selectivity to HCAL (**4**) at complete CAL conversion after 10 min, TOF 4.81 s^{-1}). The selectivity for HCAL remains high during the first hour; afterward, the acetalization of HCAL to HCDA begins, progressing slowly over time (10% HCDA formed after 8 h). No traces of HCOL are detected during the 8 h hydrogenation process, confirming once again that 0.5Pd/Ti_2/UVM-7 catalyst has an enhanced selectivity toward HCAL.

2.2.3 Influence of the support. The catalysts prepared *via* the *one-step* or the *two-step procedure* were evaluated for the hydrogenation reaction of CAL under identical reaction conditions. Results indicate that the 0.5Pd/Ti_2@UVM-7 catalyst promotes both acetalization and hydrogenation reactions, whereas the 0.5Pd/Ti_2/UVM-7 (*two-step procedure*) is very active for CAL hydrogenation to HCAL and exhibits stability over time.

The differences observed between the two supports might be a consequence of the size and the good dispersion of the Pd NPs. For the 0.5Pd/Ti_2@UVM-7 catalyst, larger Pd NPs are formed, as evidenced by XRD and TEM analyses. In contrast, the 0.5Pd/Ti2/UVM-7 features well-dispersed Pd NPs (<2 nm). In our previous study,[47] we demonstrated that a very low amount of well-dispersed Pd NPs are particularly reactive and selective for hydrogenation reactions, which aligns with enhanced HCAL selectivity observed for 0.5Pd/Ti_2/UVM-7. Moreover, the higher acidity of Ti_2@UVM-7 (as confirmed by NH_3-TPD) contributes to undesired acetalization, promoting parallel side reactions during CAL hydrogenation.

For small Pd nanoparticles (≤3 nm), the high surface curvature and abundance of low-coordination sites allow cinnamaldehyde to adsorb in a relatively flat configuration, enabling simultaneous interaction of both the C=C and C=O bonds with the metal surface. In this configuration, the C=C bond interacts more strongly with Pd due to favorable π-back-bonding and d-band interactions, making its hydrogenation kinetically preferred.[13] As a result, small Pd particles typically promote C=C hydrogenation, leading to higher selectivity toward HCAL.

In contrast, larger Pd particles (3–8 nm or larger) exhibit flatter surfaces with more extended terrace sites. Due to steric constraints imposed by the aromatic ring of cinnamaldehyde, the molecule cannot easily adopt a flat adsorption geometry on these surfaces. Instead, it preferentially adsorbs in a tilted or through the carbonyl group. This favors activation of the C=O bond and enhances selectivity toward cinnamyl alcohol rather than HCAL.[11,48–50]

To better understand the role of the support in the CAL hydrogenation in ethanol, 0.5Pd/UVM-7 and 0.5Pd/TiO_2 were also tested, and the results are gathered in Fig. 4c, d and Table S6.

When TiO_2 serves as support (Fig. 4c), CAL hydrogenation proceeds at a slower rate, reaching full conversion after 4 h, in contrast to 0.5Pd/UVM-7, which achieves complete conversion in merely 1 h (Fig. 4d). In the presence of 0.5Pd/TiO_2 catalyst, both CAL acetalization to CDA (reaction (**1**)) and subsequent hydrogenation of CDA to HCDA (reaction (**2**)) occur within the initial 2 h. This behavior is similar to that of 0.5Pd/Ti_2@UVM-7, indicating a reduced rate of CAL to HCAL hydrogenation and a greater tendency of the support to promote acetalization.

Using UVM-7 as support avoids the acetalization reaction, achieving a conversion of 97% within the initial 30 minutes and an HCAL selectivity of 94%. The conversion reaches its peak after one hour, exhibiting a selectivity of 93%.

Initial HCAL selectivity obtained for 0.5Pd/TiO_2 is 85% and decreases rapidly in time due to the fast acetalization process of HCAL to HCDA (reaction (**3**)), which was also observed for 0.5Pd/Ti_2@UVM-7 catalyst. These findings indicate that in the presence of materials containing a higher amount of TiO_2 entities, more H^+ species are generated, species that can facilitate the acetalization process. These observations are sustained also by the structural characterization of the catalysts/supports (TEM, SEM, XPS, ^{29}Si NMR) where a larger amount of Ti species was found for the Ti_2@UVM-7 based materials related to Ti_2/UVM-7 based catalysts and an increased acidic character was evidenced for Ti_2@UVM-7 support (NH_3-TPD) compared with the Ti_2/UVM-7 and UVM-7 supports.

Also, in the case of 0.5Pd/TiO_2 or 0.5Pd/UVM-7 catalysts (Fig. 4d), the hydrogenation reaction of HCAL to HCOL (**5**) can be observed since the beginning (10 min reaction time) and high HCOL yields are obtained after 24 h (42% and 20%,

respectively – Table S6) compared with the other investigated materials. This behavior is owed to the formation of larger Pd NPs (30 nm, respectively 35 nm)[11,48,50,51] on these catalysts, as determined from TEM.

There is evidence in the literature proving that Pd NPs can be stabilized on supports like SiO_2 in the presence of TiO_2 species; herein, TiO_{2-x} layer can be formed at the surface of metal clusters for Pd/TiO_2 catalysts reduced at high temperatures, responsible for a strong metal-support interaction.[52] Thus, the *two-step procedure* material could be more appropriate support for the Pd, where TiO_2 nanodomains located inside the mesopores can stabilize and prevent Pd NPs sintering at high reduction temperature (400 °C), leading to very small Pd NP. This allows for stronger electronic interactions in MSI, which is also supported by the XPS analysis. In contrast, the *one-step procedure* material has the TiO_2 species embedded into the SiO_2 matrix, a fact which favors the formation of larger Pd NPs, with less interfacial area relative to their volume, therefore the proportion of atoms at the metal-support interface decreases and consequently also the MSI.

When Pd is deposited on Ti_2/UVM-7 (*two-step procedure* support) and UVM-7 supports, where Ti species are in lower amounts or absent, respectively, the aldehyde hydrogenation is the main reaction. Nevertheless, the Pd particle size makes the difference for these catalysts, since for small Pd NPs (<2 nm) only CAL hydrogenation to HCAL occurs, while for larger Pd NPs (around 30 nm) further HCAL to HCOL hydrogenation also takes place. For the considered Pd-based systems, smaller nanoparticles expose a higher fraction of low-coordination sites (edges and corners),[2] which might favor π-bond interaction with the C=C group of cinnamaldehyde, thereby promoting selective hydrogenation toward hydrocinnamaldehyde. In contrast, larger particles may alter the adsorption geometry and facilitate competing pathways, including C=O hydrogenation or over-hydrogenation.

Even though the SSA of the 0.5Pd/Ti_2/UVM-7 catalyst is smaller compared to the 0.5Pd/Ti_2@UVM-7, it is still high enough to ensure its high catalytic performance. Therefore, the outstanding HCAL selectivity at complete CAL conversion obtained in the presence of 0.5Pd/Ti_2/UVM-7 is a contribution of MSI due to a very good dispersion of small Pd NPs (<2 nm particle sizes, according to TEM data), making it very active and selective for HCAL in the cinnamaldehyde hydrogenation process. The maximum HCAL selectivity ~99% is obtained in the first 10 minutes of the reaction, after that, other processes being favored, as HCAL acetalization to HCDA or further HCAL reduction to HCOL.

Moreover, even if Fig. 4b and d present a similar trend, the improved catalytic behavior of 0.5Pd/Ti_2/UVM-7 compared with 0.5Pd/UVM-7 can be attributed to the promoting role of Ti species, which strengthens metal-support interactions and modifies the electronic and structural properties of Pd.

2.2.4 Stability tests. Stability tests were carried out in the presence of the best catalyst, 0.5Pd/Ti_2/UVM-7, over 5 consecutive reaction cycles, each lasting 1 h (0.1 mmoles of CAL, 10 mg of catalyst, 5 mL of ethanol, 140 °C, 25 atm H_2) and the results are depicted in Fig. 5. The catalyst exhibits high stability during the first two catalytic cycles, maintaining CAL conversion at

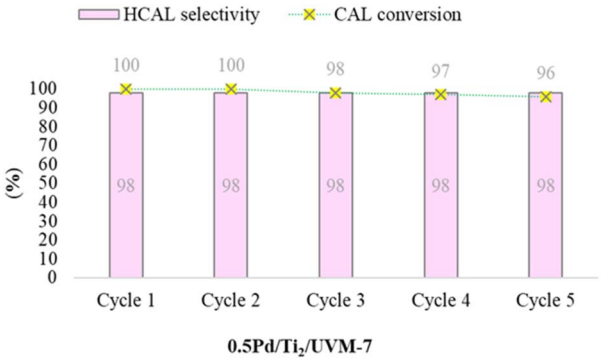

Fig. 5 Stability tests for 0.5Pd/Ti_2/UVM-7 during 5 consecutive reaction cycles.

100% and initial HCAL selectivity of ~99%. Following the third reaction cycle, a small decrease (overall less than 4%) in CAL conversion is noted.

Hot filtration tests were conducted on the 0.5Pd/Ti_2/UVM-7 catalyst to assess the potential presence of homogeneous Pd species in the reaction medium. The reaction was stopped after 7 minutes, at 85% CAL conversion. Following hot filtration, no further hydrogenation of CAL was observed in the second reaction cycle. These results indicate that no leached Pd species are present in the reaction solution during the catalytic tests.

3 Experimental

3.1 Support preparation (see Scheme 3)

3.1.1 Preparation of Ti2@UVM-7 by *one-step procedure*.[30] Herein, tetraethoxysilane (TEOS) (6.94 g), tetrabutyl orthotitanate (TBOT, 0.18 g) and triethylamine (TEA, 22.6 g) were vigorously stirred, and the mixture was heated at 140 °C. The obtained solution was cooled to 120 °C, and cetyltrimethylammonium bromide (CTAB, 3.04 g) was added. The solution was cooled down to 85 °C, and then water was added (60 mL). Further, the suspension was maintained under magnetic stirring for 16 h at room temperature (RT). The obtained solid was separated by filtration and washed thoroughly with water. The final material was calcined using a heating ramp until 550 °C, as described in Scheme S1 (see Supplementary material). The molar ratio between TEOS : TBOT:TEA : CTAB : H_2O was 2 : 0.03 : 9.1 : 0.5 : 200. The final loading of TiO_2 on UVM-7 is 2% and the sample was named Ti_2@UVM-7.

3.1.2 Preparation of Ti_2/UVM-7 by *two-step procedure*. The first step involves the synthesis of the pure silica UVM-7 *via* atrane method[53] (10 g), where UVM-7 defines a mesoporous bimodal silica. Initially, TEOS (36.9 mL) and TEA (76.9 mL) were stirred vigorously and heated at 140 °C. The obtained solution was cooled to 120 °C and CTAB (15.16 g) was added under continuous stirring. Further, the solution was cooled down to 85 °C and water (300 mL) was added. The molar ratio between TEOS : TEA:CTAB : H_2O is 2 : 7 : 0.5 : 200. The resulting precipitate was filtered, washed thoroughly with water and ethanol, and dried at 70 °C overnight. The powder was calcined using the same conditions as for the *one-step procedure*.

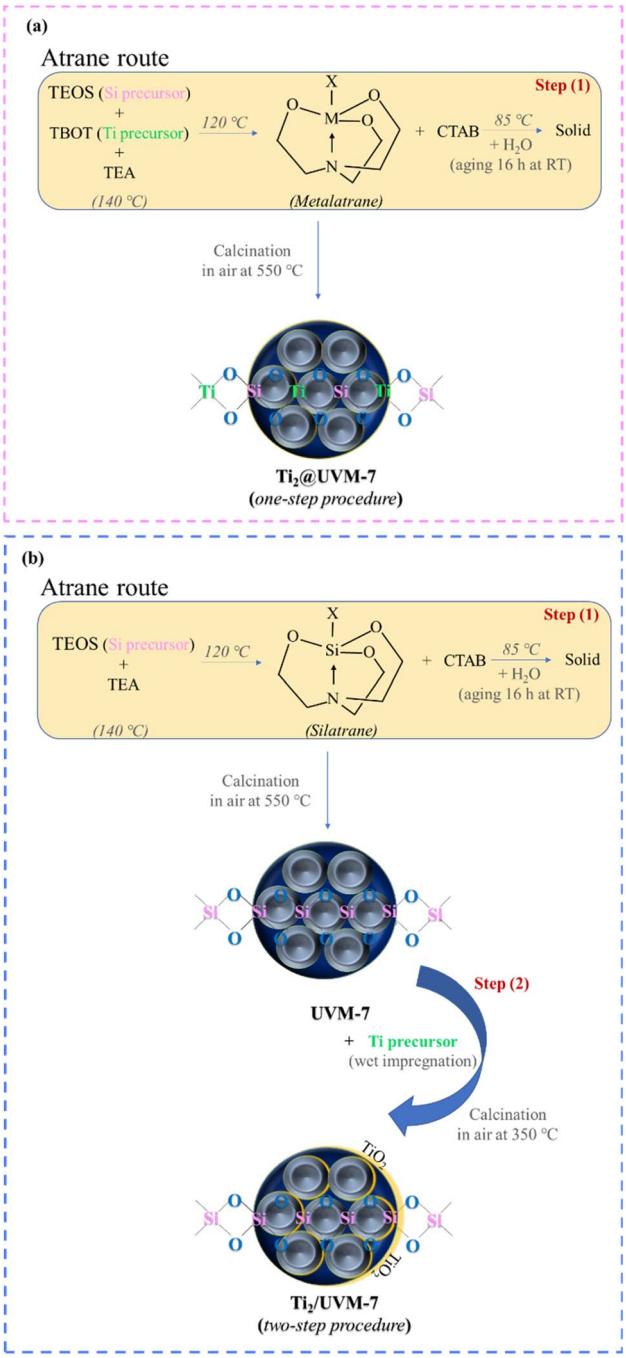

Scheme 3 The general concept for the synthesis UVM-7 based supports containing 2% TiO_2 *via* (a) *one-step procedure* to obtain Ti_2@UVM-7 support and (b) *two-step procedure* to generate Ti_2/UVM-7 support.

The second step of the synthesis involves wet impregnation of TiO_2 on UVM-7 (1 g). Titanium oxyacetylacetonate (0.06 g, used as Ti precursor) was dissolved in ethanol (100 mL, heated at 40 °C). Subsequently, water (100 mL, heated at 40 °C) was added to the solution, and the UVM-7 support (0.98 g) was slowly integrated into the reaction mixture. The suspension was held under magnetic stirring for 2 h at 40 °C. The resulting mixture was cooled at RT, the solid was separated by filtration and washed with water. The obtained material was calcined in air at 300 °C for 5 h (heating rate 1 °C min^{-1}). The final loading of TiO_2 on UVM-7 is 2%, therefore, for simplicity, the sample was named Ti_2/UVM-7.

3.2 Catalysts preparation

The catalyst was obtained by deposition–precipitation of 0.5 wt% Pd on the synthesized supports. For that purpose, $[Pd(OAc)_2]_n$ (0.005 g) was dissolved in methanol (20 mL of methanol heated at 40 °C) and added to warm water (70 °C, 40 mL). The support (Ti_2/UVM-7 or Ti_2@UVM-7) was added (1 g) and the pH was adjusted and maintained at pH = 7 with NH_4OH 25%. The mixture was vigorously stirred for 1 h at 70 °C. The obtained suspension was filtered and the solid was thoroughly washed with water. The solid was dried at 90 °C overnight, and the final materials were reduced in a flow of 5 vol% H_2 diluted in Ar (20 mL min^{-1}) at 400 °C for 3 h. Final catalysts were named 0.5Pd/Ti_2@UVM-7 and 0.5Pd/Ti_2/UVM-7. A sketch of the overall process is depicted in Scheme 4. For comparison, 0.5 wt% Pd supported on UVM-7 and TiO_2 (commercially P25, Degussa) catalysts were prepared using the same deposition precipitation method described above. The samples were named 0.5Pd/UVM-7 and 0.5Pd/TiO_2.

3.3 Catalyst characterization

The structure of the catalysts was investigated by X-ray diffraction (XRD) using an Anton Paar XRDynamic 500 diffractometer equipped with CuK_α ($\lambda K\alpha 1$ = 1.5418 Å, 40 kV, 50 mA) Primux 3000 X-rays source and one-dimensional Pixos 2000 detector. The patterns were registered with parallel beam optics in the 2θ range 1.2–18° with a step size of 0.02° and between 10–70° with a step size of 0.04°; the crystalline planes of the materials were identified according to the ICDD crystallographic database. The crystallite sizes were evaluated from line broadening according to the Scherrer equation:[54,55]

Crystallite size (nm) = λ/(FWHM*cos θ), where λ = 0.15418 nm (CuK_α), FWHM is full width at half maximum, and θ is the diffraction angle.

The chemical structure and presence of functional groups were investigated by Fourier-transform infrared (FTIR) spectroscopy using a PerkinElmer spectrometer in attenuated total reflectance (ATR) mode with a diamond crystal plate device (Pike Technologies, Madison, WI). The IR absorption spectra of the all samples were recorded from 500 to 4000 cm^{-1} at a nominal resolution of 4 cm^{-1} and 32 scans/acquisition.

Nitrogen physisorption analysis was performed at −196 °C with a 3FLEX apparatus from Micromeritics. Before determining the surface area, all powders were degassed at 200 °C for 1 h. The Brunauer–Emmett–Teller (BET) formalism[56] was used to calculate the specific surface area from the data obtained at P/P_0 between 0.025 and 0.3. The pore size distribution of each sample was determined from the desorption branch of the N_2 isotherm, while the pore size and volume analysis were calculated using the Barrett–Joyner–Halenda (BJH) formalism.[57]

The morphology and elemental composition of the samples have been studied with:

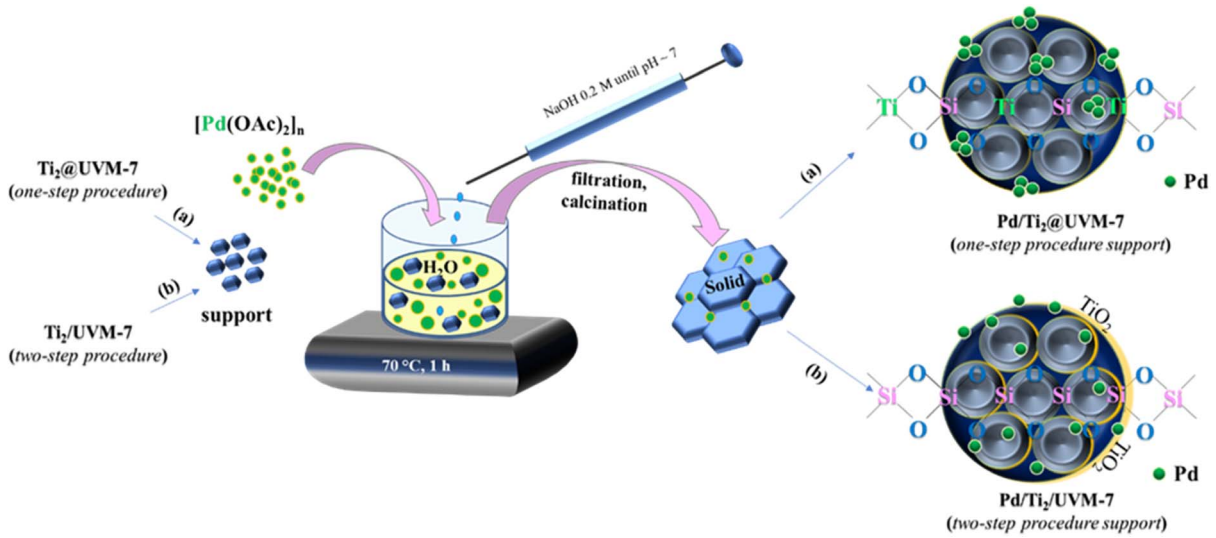

Scheme 4 Schematic representation of Pd deposition precipitation on (a) Ti_2@UVM-7 *one-step procedure* support and (b) Ti_2/UVM-7 *two-step procedure* support.

(i) JEOL2100 Transmission Electron Microscope (TEM), equipped with a JEOL Energy Dispersive X-ray (EDX) Spectrometer. Prior to the analysis, the samples were well grounded and dispersed into ethanol; the slurry was dropped onto a copper grid and allowed to dry at RT. Conventional imaging (CTEM) as well as scanning imaging obtained in dark-field operation mode (STEM-DF) showed spherical particles with sizes under 50 nm. The EDX analyses were performed in three different regions of each sample.

(ii) Zeiss Evo 50 XVP scanning electron microscope (SEM) coupled with a spectrometer of energy dispersion of X-ray (EDX) Bruker Quantax 200. The operational parameters used for the SEM images and EDX analyses were: accelerating voltage 20 kV, measuring time 300 s and working distance around 17 mm.

The XPS measurements were recorded using a Kratos XPS Axis Ultra DLD Setup spectrometer with the Al K_α (1486.74 eV) radiation generated by an X-ray source operating at 144 W (12 kV, 12 mA) and a vacuum of 1×10^{-4} MPa. The photoelectrons emitted were detected using a 165 mm radius hemispherical energy analyzer operating in a fixed analyzer transmission mode with a pass energy of 20 eV and a magnetic immersion lens to improve electron detection efficiency. An electron flood gun running at 1 eV electron energy and a 0.1 mA current was employed to counteract sample charging effects. The parameters were adjusted to achieve the adventitious C 1s peak at 285 ± 0.05 eV.

NH_3-Temperature Programmed Desorption (NH_3-TPD) experiments were carried out in a Micromeritics TriFlex equipment. The samples (100 mg) were pretreated at 100 °C (from RT with a 5 °C min^{-1} heating rate) under He flow (20 mL min^{-1}) during 1 h to clean the surface. The material was cool down at RT and cured with a 5% NH_3 in He gas mixture (20 mL min^{-1}) for 1 h. Subsequently, the samples were exposed to He (20 mL min^{-1}) for 1 h to remove the physically adsorbed CO_2 and finally treated from RT up to 550 °C (heating rate 10 °C min^{-1}) and the desorbed NH_3 was quantified by a TCD detector.

Solid-state ^{29}Si MAS NMR experiments were performed on a 9.39 T spectrometer (400 MHz for ^1H) equipped with a magic-angle spinning (MAS) probe. The ^{29}Si spectra were acquired using single-pulse excitation under MAS conditions at a spinning rate of 10 kHz, 18 000 scans, employing 4 mm zirconia rotors fitted with Kel-F caps. Chemical shifts were referenced to an external kaolin standard.

3.4 Catalytic tests

The hydrogenation of CAL was carried out in a stainless-steel autoclave under magnetic stirring. In a standard experiment, the catalyst (10 mg) was mixed with the substrate (0.0132 g, 0.1 mmol) and ethanol (5 mL) in the autoclave that was initially flushed three times with H_2, after that pressurized with H_2 at 25 atm. The reactions were carried out at 140 °C for 0.16–24 h. After the reaction, the catalyst was separated by filtration, and the reaction products were analyzed by gas chromatography (GC) coupled with a quadrupole mass spectrometer (MS; Shimadzu GC-MS-QP2010 Ultra GC-MS) equipped with an Elite 35 MS column (30 m, 0.5 μm thickness, diameter 0.25 mm). The GC conditions for sample analysis were as follows: injector temperature 250 °C, carrier gas – helium (3 mL min^{-1}), pressure 0.11 atm, linear velocity 23.2 cm sec^{-1}, oven temperature – starting at 120 °C (hold 4 min) then increasing with a heating rate of 20 °C min^{-1} up to 275 °C and hold 20 min, detector MS(EI), ion source temperature 200 °C, interface temperature 275 °C and detector voltage 0.1 kV. The catalytic results are presented in terms of cinnamaldehyde conversion (C%) and reaction products selectivity (S(%)):

$$C\% = \frac{\text{initial CAL (wt\%)} - \text{CAL after reaction (wt\%)}}{\text{initial CAL (wt\%)}} \times 100$$

$$S(\%) = \frac{\text{amount of product (wt\%)}}{\text{amount of all products (wt\%)}} \times 100$$

The apparent Turnover frequency (TOF) is defined as the ratio of the mole number of converted CAL to the mole number of accessible Pd (considering the Pd NP size determined from TEM) in time and was reported as s^{-1}.

The recyclability of the best catalyst was evaluated using a single batch over 5 consecutive reaction cycles. After each reaction, the mixture was allowed to settle, and the liquid was carefully extracted using a syringe; aliquots were diluted with ethanol and subsequently injected into the GC-MS, while the catalyst underwent washing with ethanol. A fresh batch of solvent and CAL mixture is further added to the catalyst for the next cycle, up to 5 reaction cycles (0.1 mmol CAL, 5 mL EtOH, 140 °C, 25 atm H_2, 1 h).

The hot filtration test was carried out as follows: a standard reaction cycle was performed, but the reaction was stopped after 7 minutes of reaction time (at 85% CAL conversion). After the standard reaction cycle, the hot reaction mixture was filtered to remove the catalyst and returned to the batch reactor The reactor was sealed, flushed (three times) and pressurized with 25 atm H_2 and heated to 140 °C for 10 minutes. The reaction products were also analyzed by GC-MS.

4 Conclusions

For this study, 0.5 wt% Pd were deposited on bimodal mesoporous supports – (2 wt%) TiO_2–SiO_2 – with high SSA (>900 $m^2 g^{-1}$). During the deposition–precipitation step of Pd, the structure of the support was well-preserved for the *one-step procedure*, most likely due to the generation of a higher amount of Ti–O–Si bonds, as evidenced by ATR-FTIR, XPS and ^{29}Si NMR measurements, while for the *two-step procedure*, the textural properties of the support were slightly affected by the partial collapse of the structure or pore blocking with Pd NP, as observed from the XRD and SSA results. However, very small Pd NP sizes (<2 nm) were obtained for the *two-step procedure* support, which determined a strong MSI as evidenced by XPS.

Catalytic tests revealed competing pathways during CAL hydrogenation: direct CAL hydrogenation to HCAL and subsequent acetalization to CDA/HCDA. These parallel reactions were more pronounced for *one-step procedure* catalyst (0.5Pd/Ti_2@UVM-7). Catalysts containing higher TiO_2 concentrations promoted both hydrogenation and acetalization, lowering HCAL yield, while Pd/SiO_2 exhibited complete CAL conversion with high HCAL selectivity (~93%).

The 0.5Pd/Ti_2/UVM-7 catalyst prepared by a *two-step procedure* achieved nearly 99% HCAL selectivity at full CAL conversion within 10 minutes with a TOF of 4.81 s^{-1}, among the highest reported values.[2] This catalytic performance originates from the ultrasmall Pd nanoparticles in strong electronic and structural coupling with the support, evidencing a pronounced metal–support interaction.

Author contributions

The manuscript was written by all authors. MMT – catalysts preparation; catalytic reaction; validation; writing the original draft, conceptualization, review and editing, data interpretation, methodology, project administration; AGM – catalysts preparation; catalytic reaction, data interpretation, methodology; IMC – XRD and FTIR analysis; methodology, writing and data interpretation; FN – XPS analysis and data interpretation; SN – FTIR analysis and data interpretation; AGM and ICC – Solid state NMR analysis and data interpretation; CR – TEM analysis; MF – conceptualization, data interpretation, writing, review and editing. All authors have given approval to the final version of the manuscript.

Conflicts of interest

The information and views set out in this article are those of the author NF, and do not necessarily reflect the official opinion of the European Commission and ERCEA.

Data availability

The data supporting the article been provided as part of the supplementary information (SI). Supplementary information is available. See DOI: https://doi.org/10.1039/d6ta00748a.

Acknowledgements

This work was supported by a grant of the Romanian Ministry of Research, Innovation and Digitalization, CNCS-UEFISCDI, project number PN-III-P1-1.1-PD-2019-1092 (contract no. 77), within PNCDI III. The Core Program 2023–2026 (contract PC3-PN23080303) is also gratefully acknowledged.

References

1 V. I. Isaeva, M. D. Vedenyapina, S. A. Kulaishin, A. A. Lobova, V. V Chernyshev, G. I. Kapustin, O. P. Tkachenko, V. V Vergun, D. A. Arkhipov, V. D. Nissenbaum and L. M. Kustov, *Dalton Trans.*, 2019, **48**, 15091–15104.
2 X. Wang, X. Liang, P. Geng and Q. Li, *ACS Catal.*, 2020, **10**, 2395–2412.
3 M. C. Bryan, P. J. Dunn, D. Entwistle, F. Gallou, S. G. Koenig, J. D. Hayler, M. R. Hickey, S. Hughes, M. E. Kopach, G. Moine, P. Richardson, F. Roschangar, A. Steven and F. J. Weiberth, *Green Chem.*, 2018, **20**, 5082–5103.
4 P. Mäki-Arvela, J. Hájek, T. Salmi and D. Y. Murzin, *Appl. Catal., A*, 2005, **292**, 1–49.
5 C. S. Letizia, J. Cocchiara, J. Lalko, A. Lapczynski and A. M. Api, *Food Chem. Toxicol.*, 2005, **43**, 837–866.
6 A. Sreenavya, C. N. Mallannavar and A. Sakthivel, *Mater. Today Proc.*, 2021, **46**, 3152–3157.
7 R. Li, W. Yao, Y. Jin, W. Jia, X. Chen, J. Chen, J. Zheng, Y. Hu, D. Han and J. Zhao, *Chem. Eng. J.*, 2018, **351**, 995–1005.

8 M. Gopiraman, S. G. Babu, Z. Khatri, K. Wei, M. Endo, R. Karvembu and I. S. Kim, *Catal. Sci. Technol.*, 2013, **3**, 1485–1489.
9 S. P. Bhatia, G. A. Wellington, J. Cocchiara, J. Lalko, C. S. Letizia and A. M. Api, *Food Chem. Toxicol.*, 2011, **49**, S246–S251.
10 A. Muller and J. Bowers, First Chemical Corporation, *WO Patent*, WO 99/08989, 1999.
11 A. J. Plomp, H. Vuori, A. O. I. Krause, K. P. de Jong and J. H. Bitter, *Appl. Catal., A*, 2008, **351**, 9–15.
12 C. Mohr and P. Claus, *Sci. Prog.*, 2001, **84**, 311–334.
13 E. Bailón-García, F. J. Maldonado-Hódar, A. F. Pérez-Cadenas and F. Carrasco-Marín, *Catalysts*, 2013, **3**, 853–877.
14 P. Gallezot and D. Richard, *Catal. Rev.*, 1998, **40**, 81–126.
15 S. Gryglewicz, A. Śliwak, J. Ćwikła and G. Gryglewicz, *Catal. Lett.*, 2014, **144**, 62–69.
16 T. Yuan, D. Liu, Y. Pan, X. Pu, Y. Xia, J. Wang and W. Xiong, *Catal. Lett.*, 2019, **149**, 851–859.
17 L. Liu, P. Concepción and A. Corma, *J. Catal.*, 2016, **340**, 1–9.
18 B. Li and H. C. Zeng, *ACS Appl. Mater. Interfaces*, 2018, **10**, 29435–29447.
19 K. N. Patil, P. Manikanta, P. M. Srinivasappa, A. H. Jadhav and B. M. Nagaraja, *J. Environ. Chem. Eng.*, 2023, **11**, 109168.
20 L. Chen, H. Chen and Y. Li, *Chem. Commun.*, 2014, **50**, 14752–14755.
21 T. Hu, L. Zhang, Y. Wang, Z. Yue, Y. Li, J. Ma, H. Xiao, W. Chen, M. Zhao, Z. Zheng and J. Jia, *ACS Sustain. Chem. Eng.*, 2020, **8**, 7851–7859.
22 F. Delbecq and P. Sautet, *J. Catal.*, 1995, **152**, 217–236.
23 M. M. Trandafir, A. Moragues, P. Amorós and V. I. Parvulescu, *Catal. Today*, 2020, **355**, 893–902.
24 X. Li, J. Liu, J. Wu, L. Zhang, D. Cao and D. Cheng, *ACS Catal.*, 2024, **14**, 2369–2379.
25 M. Pérez-Cabero, F. R. García-García, D. Vie, I. Rodríguez-Ramos, D. Beltrán and P. Amorós, *Mater. Lett.*, 2008, **62**, 2935–2938.
26 E. Tronconi, C. Crisafulli, S. Galvagno, A. Donato, G. Neri and R. Pietropaolo, *Ind. Eng. Chem. Res.*, 1990, **29**, 1766–1770.
27 B. Puértolas, Á. Mayoral, R. Arenal, B. Solsona, A. Moragues, S. Murcia-Mascaros, P. Amorós, A. B. Hungría, S. H. Taylor and T. García, *ACS Catal.*, 2015, **5**, 1078–1086.
28 M. Ródenas, J. El Haskouri, J. V Ros-Lis, M. D. Marcos, P. Amorós, M. Á. Úbeda and F. Pérez-Pla, *Catalysts*, 2020, **10**, 449–467.
29 M. Pérez-Cabero, A. B. Hungría, J. M. Morales, M. Tortajada, D. Ramón, A. Moragues, J. El Haskouri, A. Beltrán, D. Beltrán and P. Amorós, *J. Nanoparticle Res.*, 2012, **14**, 1045.
30 A. Moragues, B. Puértolas, Á. Mayoral, R. Arenal, A. B. Hungría, S. Murcia-Mascarós, S. H. Taylor, B. Solsona, T. García and P. Amorós, *J. Catal.*, 2018, **360**, 187–200.
31 C. M. Opriş, O. D. Pavel, A. Moragues, J. El Haskourib, D. Beltrán, P. Amorós, M. D. Marcos, L. E. Stoflea and V. I. Parvulescu, *Catal. Sci. Technol.*, 2014, **4**, 4340–4355.
32 E. Lalik, A. Drelinkiewicz, R. Kosydar, R. Tokarz-Sobieraj, M. Witko, T. Szumełda, J. Gurgul and D. Duraczyńska, *Appl. Catal., A*, 2016, **517**, 196–210.
33 V. A. Zeitler and C. A. Brown, *J. Phys. Chem.*, 1957, **61**, 1174–1177.
34 K. V. Kumar, C. Valenzuela-Calahorro, J. M. Juarez, M. Molina-Sabio, J. Silvestre-Albero and F. Rodriguez-Reinoso, *Chem. Eng. J.*, 2010, **162**, 424–429.
35 G. Lassaletta, A. Caballero, S. Wu, A. R. González-Elipe and A. Fernández, *Vacuum*, 1994, **45**, 1085–1086.
36 S. Chen, L. Meng, B. Chen, W. Chen, X. Duan, X. Huang, B. Zhang, H. Fu and Y. Wan, *ACS Catal.*, 2017, **7**, 2074–2087.
37 X. Zhu, Q. Guo, Y. Sun, S. Chen, J.-Q. Wang, M. Wu, W. Fu, Y. Tang, X. Duan, D. Chen and Y. Wan, *Nat. Commun.*, 2019, **10**, 1428.
38 Z. Jiang, Y. Li, Z. Tang, D. Yuan and F. Lin, *Environ. Sci. Technol.*, 2025, **59**, 19644–19666.
39 E. Paparazzo, M. Fanfoni, E. Severini and S. Priori, *J. Vac. Sci. Technol., A*, 1992, **10**, 2892–2896.
40 F. Hou, R. Gorthy, I. Mardon, D. Tang and C. Goode, *Sci. Rep.*, 2022, **12**, 6037.
41 X. Gao and I. E. Wachs, *Catal. Today*, 1999, **51**, 233–254.
42 K. Kosuge, *J. Phys. Chem. B*, 1999, **103**, 3563–3569.
43 L. Zhang, J. M. Winterbottom, A. P. Boyes and S. Raymahasay, *J. Chem. Technol. Biotechnol.*, 1998, **72**, 264–272.
44 J. Hájek, N. Kumar, P. Mäki-Arvela, T. Salmi, D. Y. Murzin, I. Paseka, T. Heikkilä, E. Laine, P. Laukkanen and J. Väyrynen, *Appl. Catal., A*, 2003, **251**, 385–396.
45 M. Lashdaf, M. Tiitta, T. Venäläinen, H. Österholm and A. O. I. Krause, *Catal. Lett.*, 2004, **94**, 7–14.
46 Y. Bai, N. Cherkasov, S. Huband, D. Walker, R. I. Walton and E. Rebrov, *Catalysts*, 2018, **8**, 58–76.
47 M. M. Trandafir, F. Neaţu, I. M. Chirica, Ş. Neaţu, A. C. Kuncser, E. I. Cucolea, V. Natu, M. W. Barsoum and M. Florea, *ACS Catal.*, 2020, **10**, 5899–5908.
48 R. C. J. van de Poll, H. Friedrich and E. J. M. Hensen, *Catal. Sci. Technol.*, 2025, **15**, 765–773.
49 F. Jiang, J. Cai, B. Liu, Y. Xu and X. Liu, *RSC Adv.*, 2016, **6**, 75541–75551.
50 A. Giroir-Fendler, D. Richard and P. Gallezot, *Catal. Lett.*, 1990, **5**, 175–181.
51 F. Jiang, J. Cai, B. Liu, Y. Xu and X. Liu, *RSC Adv.*, 2016, **6**, 75541–75551.
52 M. Lu, J. Zhu, M. Li, Y. Shan, M. He and C. Song, *Energy Fuels*, 2016, **30**, 6671–6676.
53 S. Cabrera, J. El Haskouri, C. Guillem, J. Latorre, A. Beltrán-Porter, D. Beltrán-Porter, M. D. Marcos and P. Amorós *, *Solid State Sci.*, 2000, **2**, 405–420.
54 G. Ertl, H. Knözinger and J. Weitkamp, *Handbook of Heterogeneous Catalysis*, VCH Wiley Company, 1997, vol. 2.
55 H. P. Klug and L. E. Alexander, *X-Ray Diffraction Procedures: for Polycrystalline and Amorphous Materials*, John Wiley & Sons, 2nd edn, 1974.
56 S. Brunauer, P. H. Emmett and E. Teller, *J. Am. Chem. Soc.*, 1938, **60**, 309–319.
57 E. P. Barrett, L. G. Joyner and P. P. Halenda, *J. Am. Chem. Soc.*, 1951, **73**, 373–380.

